

**Measurement of Hadron and Lepton-Pair Production
at $130 \text{ GeV} < \sqrt{s} < 140 \text{ GeV}$ at LEP**

The L3 Collaboration

Abstract

We report on the first measurements of e^+e^- annihilations into hadrons and lepton pairs at centre-of-mass energies between 130 GeV and 140 GeV. In a total luminosity of 5 pb^{-1} collected with the L3 detector at LEP we select 1577 hadronic and 401 lepton-pair events. The measured cross sections and leptonic forward-backward asymmetries agree well with the Standard Model predictions.

Submitted to *Physics Letters B*

1 Introduction

Until October 1995 the LEP collider was operated at centre-of-mass energies around the Z resonance and produced about 4 million Z decays for each of the four experiments. This large data sample allows an accurate determination of the Z boson properties and thus a precise test of the Standard Model of electroweak interactions [1].

In November 1995 LEP was operated for the first time at energies well above the Z resonance. During this run the L3 detector has collected a total integrated luminosity of 5 pb^{-1} at centre-of-mass energies, \sqrt{s} , between 130 GeV and 140 GeV. In this article we report on the measurements of the reactions:

$$\begin{aligned} e^+e^- &\rightarrow \text{hadrons}(\gamma) & e^+e^- &\rightarrow \mu^+\mu^-(\gamma) & e^+e^- &\rightarrow \tau^+\tau^-(\gamma) \\ e^+e^- &\rightarrow e^+e^-(\gamma) & e^+e^- &\rightarrow \nu\bar{\nu}\gamma(\gamma) \end{aligned}$$

at these centre-of-mass energies. We measure cross sections for all reactions and forward-backward asymmetries for the charged lepton final states.

In these reactions, the (γ) indicates the possible presence of additional photons. For a large fraction of the events, initial-state radiation (ISR) photons lower the effective centre-of-mass energy, $\sqrt{s'}$, of the annihilation process to values close to the Z mass, m_Z ('radiative return to the Z'). A cut on $\sqrt{s'}$ allows us to determine the exclusive cross sections and asymmetries for high energy events, $\sqrt{s'} > m_Z$. The measurements are compared to the predictions of the Standard Model. Together with our Z measurements [2], they are used to determine the properties of the Z boson in the framework of the S-Matrix ansatz [3,4]. High energy measurements are in particular sensitive to the parameters describing the interference between photon and Z exchange.

2 The L3 Detector

The L3 detector [5] consists of a silicon microstrip detector [6], a central tracking chamber, a high resolution electromagnetic calorimeter composed of BGO crystals, a lead-scintillator ring calorimeter at low polar angles [7], a scintillation counter system, a uranium hadron calorimeter with proportional wire chamber readout, and an accurate muon chamber system. A forward-backward muon detection system extends the polar angle coverage of the muon chambers down to 24 degrees in the forward-backward region [8]. These detectors are installed in a 12 m diameter magnet which provides a solenoidal field of 0.5 T and a toroidal field of 1.2 T. The luminosity is measured using BGO calorimeters preceded by silicon trackers [9] situated on each side of the detector.

The response of the L3 detector is modelled with the GEANT [10] detector simulation program which includes the effects of energy loss, multiple scattering and showering in the detector materials and in the beam pipe.

3 Measurement of Fermion-Pair Production

Hadronic and leptonic final states produced in e^+e^- annihilations are analysed at centre-of-mass energies of 130.3 GeV, 136.3 GeV and 140.2 GeV. For leptonic final states the data for the last two energies are combined because of limited luminosity at the highest energy point.

The measurement of the luminosity, \mathcal{L} , proceeds as described in [9]. For the centre-of-mass energies discussed in this paper, the uncertainty on the theoretical cross section, calculated with the BHLUMI Monte Carlo generator [11], is estimated to be at most 0.25% [12]. Other sources of systematic error are negligible.

Besides the measurement of the total cross section including all radiative effects, the most important aim of this analysis is to probe the physics at high effective centre-of-mass energies, $\sqrt{s'} > m_Z$. To separate the high energy events from the radiative return to the Z , $\sqrt{s'}$ is required to be larger than 110 GeV for all final states. For $e^+e^- \rightarrow e^+e^-(\gamma)$ the effective centre-of-mass energy is reconstructed directly from the invariant mass of the fermion system. For the other reactions $\sqrt{s'}$ is estimated from the ISR photon energy, E_γ ,

$$s' = s - 2E_\gamma\sqrt{s}. \quad (1)$$

For most of the events the ISR photon escapes along the beam pipe and is not detected. The assumption of a three-particle final state and a photon emission along the beam axis nevertheless allows the photon energy to be determined. The corrections from multiple photon radiation are estimated using Monte Carlo simulation.

Selection efficiencies and background contaminations of all processes are determined by Monte Carlo simulation performed for each centre-of-mass energy. The following Monte Carlo event generators are used to simulate the various reactions: PYTHIA [13] ($e^+e^- \rightarrow \text{hadrons}(\gamma)$, hadronic and leptonic two-photon collisions); KORALZ [14] ($e^+e^- \rightarrow \mu^+\mu^-(\gamma)$, $\tau^+\tau^-(\gamma)$, $\nu\bar{\nu}(\gamma)$); BHAGENE3 [15] ($e^+e^- \rightarrow e^+e^-(\gamma)$); NNGSTR [16] ($e^+e^- \rightarrow \nu\bar{\nu}\gamma(\gamma)$); DIAG36 [17] ($e^+e^- \rightarrow e^+e^-\mu^+\mu^-$); GGG [18] ($e^+e^- \rightarrow \gamma\gamma(\gamma)$).

The determination of systematic errors is limited by the available statistics of data and Monte Carlo. The quoted systematic errors are conservative estimates and in all cases small compared to the statistical error of the measurements.

The measurements are compared to the predictions of the Standard Model [15, 19, 20] calculated with the following parameters: $m_Z = 91.195$ GeV [2], $\alpha_s(m_Z^2) = 0.123$ [21], $m_t = 180$ GeV [22], $\alpha(m_Z^2) = 1/128.896$ [23] and $m_H = 300$ GeV.

3.1 $e^+e^- \rightarrow \text{hadrons}(\gamma)$

Event Selection

The selection criteria based on calorimetric information are the same as the ones used for the analysis of the data taken in the vicinity of the Z pole [2]. In Figure 1a the distribution of the visible energy normalised to the centre-of-mass energy is shown. The double-peak structure of the signal arises from the high energy events and the radiative return to the Z .

The photon energy for each event is reconstructed and Equation (1) is used to calculate the $\sqrt{s'}$ value. For 15% of the events with hard ISR, the photon is detected in the electromagnetic calorimeter and found by requiring electromagnetic shower shape of the cluster, an energy of more than 15 GeV and an angular separation of more than 10 degrees to the nearest energy deposition. For these photons the energy resolution is better than 2%. The other events are clustered into two jets. A kinematic fit is performed on the two jets and the missing energy vector imposing four-momentum conservation. The direction of the missing energy vector is constrained to the beam axis. As output the missing energy is obtained with a resolution of 15% and is identified with the ISR photon.

Cross Section

For all the selection variables, good agreement between data and the Monte Carlo prediction is observed. The selection efficiencies are listed in Table 1. Compared to the event selection at the Z the selection efficiency is about 4% lower due to events with hard ISR photons. The efficiency loss is caused by the cut on the visible energy, $E_{\text{vis}}/\sqrt{s} > 0.5$, and the longitudinal energy imbalance, $E_{\text{long}}/E_{\text{vis}} < 0.6$. These two cuts are not changed because they efficiently reject hadronic two-photon collisions which represent the only important background. The systematic error of the selection efficiency is dominated by these two cuts. The systematic uncertainties are summarised in Table 1 for the different event samples.

After application of the selection cuts the sample contains a small background from two-photon collisions and $e^+e^- \rightarrow \tau^+\tau^-(\gamma)$ events. The background contributions and their uncertainties for the different event samples are also summarised in Table 1. All other background sources, in particular cosmic rays and beam related backgrounds, are negligible.

The data distribution of the reconstructed $\sqrt{s'}$ is fitted by two Monte Carlo distributions. These are the reconstructed $\sqrt{s'}$ distributions for events above and below a $\sqrt{s'}$ value of 110 GeV at generator level. Binned log-likelihood fits determine the high energy cross sections for the three different centre-of-mass energies. These fits have probabilities between 6% and 55%. The systematic error of the fit procedure is estimated to be 1.3% by varying the $\sqrt{s'}$ cut value and the bin size. The distribution of the reconstructed $\sqrt{s'}$ for the 136 GeV data compared to the fitted Monte Carlo distribution is shown in Figure 1b.

A systematic error of 1.1% for the total and 1.5% for the high energy event sample is assigned to the cross section measurements. The number of selected events and the total cross sections for the different centre-of-mass energies and the different event samples are listed in Table 2 and compared to the Standard Model prediction in Figure 2.

To derive the ratio between the hadronic and leptonic cross sections for the high energy event sample, $\sqrt{s'} > 110$ GeV, the weighted average of the muon and tau-pair cross section as given in Table 2 is used. The ratio is found to be 9.7 ± 1.9 at 130 GeV and 10.1 ± 2.3 at 136 GeV, and agrees well with the Standard Model predictions of 10.2 and 9.6, respectively.

3.2 $e^+e^- \rightarrow \mu^+\mu^-(\gamma)$

Event Selection

The event selection for the process $e^+e^- \rightarrow \mu^+\mu^-(\gamma)$ requires two identified muons within the polar angular range given by the acceptance of the muon spectrometer, $|\cos\theta| < 0.9$. Muons are identified by either a reconstructed track in the muon chambers or as a minimum ionising particle in the calorimeters, as described in [2]. An event should have at least one reconstructed muon chamber track to be accepted.

The cut on the highest momentum measured in the muon chambers, p_{max} , is lowered to 50% of the beam energy to ensure high acceptance for events with hard ISR photons. The momentum distribution for the selected events is shown in Figure 3a. A cut on the acollinearity angle is applied, $\xi < 90^\circ$.

The background from cosmic rays is reduced by requiring the scintillation counters on the muon tracks to have a hit in a time window of ± 3.5 ns around the beam crossing. The difference of the two scintillation counter times should be less than 3.5 ns, equivalent to a 2.5σ separation from the expected cosmic ray signal. At least one track in the central tracking chamber is required to have a distance of closest approach to the beam axis of less than 0.5 mm.

The $\sqrt{s'}$ value is determined from the ISR photon according to Equation (1). Photons are detected in the electromagnetic calorimeter and found by requiring an energy larger than 10 GeV and an angular separation larger than 10 degrees to the nearest muon. For these events the measured photon energy is used in the calculation. In all other cases the photon energy is calculated according to:

$$E_\gamma = \sqrt{s} \cdot \frac{|\sin(\theta_1 + \theta_2)|}{\sin \theta_1 + \sin \theta_2 + |\sin(\theta_1 + \theta_2)|}, \quad (2)$$

where θ_1 and θ_2 are the polar angles of the outgoing muons. The distribution of the reconstructed $\sqrt{s'}$ is shown in Figure 3b. A cut on $\sqrt{s'}$ larger than 110 GeV isolates high energy events.

Cross Section

The selection efficiencies are listed in Table 1. Conservatively an error of 3% on detector and reconstruction efficiencies is assumed, mainly arising from the recently installed forward-backward muon chamber system.

The cosmic ray contamination is determined from the sidebands of the scintillator time distribution. The expected cosmic fraction of the final event sample is given in Table 1 and represents the most important background source. As a cross check an alternative muon-pair selection with a different cosmic rejection is performed. Both analyses give consistent results.

The background contributions, including the contamination of the high energy event sample by events with hard ISR photons, are summarised in Table 1. A systematic error of 4% for the total and 5% for the high energy sample is assigned to the cross section measurements.

Table 2 summarises the number of selected events and the resulting cross sections for the two different event samples at the different centre-of-mass energies. The cross sections are extrapolated to the full solid angle. In Figure 4 the comparison to the Standard Model prediction is shown.

Forward-Backward Asymmetry

The forward-backward asymmetry, A_{fb} , is defined as:

$$A_{fb} = \frac{\sigma_f - \sigma_b}{\sigma_f + \sigma_b},$$

where σ_f (σ_b) is the cross section for events with the fermion scattered into the hemisphere which is forward (backward) with respect to the e^- beam direction, $\cos \theta > 0$ ($\cos \theta < 0$).

The angular distribution in the region $|\cos \theta| < 0.9$ for an acollinearity angle cut of 90 degrees is approximated by the lowest-order Born formula:

$$\frac{d\sigma}{d \cos \theta} \propto \frac{3}{8}(1 + \cos^2 \theta) + A_{fb} \cos \theta. \quad (3)$$

The asymmetry is determined from an unbinned log-likelihood fit of Equation (3) to the data, where the fermion is identified by the muon charge. The effect of a wrong charge assignment on the asymmetry is negligible.

The background from $e^+e^- \rightarrow \tau^+\tau^-(\gamma)$ is small and has the same asymmetry as the signal and thus no influence on the measurement. The asymmetry of cosmic rays and two-photon collisions is consistent with zero and leads to the multiplicative correction c listed in Table 3.

In case of the high energy events, c includes the correction for the remaining background of events with hard ISR photons, as calculated from Monte Carlo.

Table 3 summarises the number of forward and backward events, the background corrections, and the corrected asymmetries. In Figure 4 the comparison of the measured asymmetries to the Standard Model prediction is shown.

3.3 $e^+e^- \rightarrow \tau^+\tau^-(\gamma)$

Event Selection

Taus are identified as narrow, low multiplicity jets. Events containing two electrons or two muons are rejected. Each event is divided into two hemispheres defined by the plane orthogonal to the thrust axis. In each hemisphere no more than three tracks in the central tracking chamber are allowed. The leading particle of the hemisphere is identified by the highest energy calorimetric cluster with an associated track, originating from the interaction point, within a cone of 10 degrees half opening angle. A ‘tau jet’ is formed summing all calorimetric clusters inside this cone. The maximum tau-jet energy is required to be greater than 15 GeV. The largest azimuthal angle between any two tracks in a hemisphere is required to be less than 15 degrees to remove background from hadronic final states. The polar angles of the two leading particles are restricted to $|\cos\theta| < 0.9$. The angle between the directions of the two leading particles is required to be greater than 90 degrees. In the region $0.72 < |\cos\theta| < 0.80$, which is not completely covered by the electromagnetic calorimeter, only events with at least one hemisphere containing three tracks are selected.

The two highest energy clusters in the electromagnetic calorimeter are required to have energies less than 80% and 45% of the beam energy to reject Bhabha background. Radiative Bhabha events and events from the two-photon collision process $e^+e^- \rightarrow e^+e^-e^+e^-$ are removed by rejecting events with two identified electrons. Electrons are identified by a cluster in the electromagnetic calorimeter with energy larger than 3 GeV, with electromagnetic shower shape, and a matched track. All events with two reconstructed tracks in the muon chambers are removed. The background from cosmic rays is reduced by requiring at least one scintillation counter to have a hit in a time window of ± 3 ns around the beam crossing.

The reconstruction of $\sqrt{s'}$ is done according to Equations (1) and (2) using the polar angles of the leading particles of both tau jets. A cut of 110 GeV isolates high energy events.

Cross Section

Selection efficiencies and background contaminations are listed in Table 1. The systematic error of the event selection is estimated to be 5%. The samples of high energy events contain a contamination of 15% and 14% from events with hard ISR photons for the 130 GeV and 136 GeV data, respectively.

The number of selected events and the total cross sections for the different centre-of-mass energies and the different event samples are listed in Table 2. The cross sections are extrapolated to the full solid angle. They are compared to the Standard Model prediction in Figure 5.

Forward-Backward Asymmetry

The forward-backward asymmetry is determined by an unbinned log-likelihood fit of Equation (3) to events with unambiguous charge assignment. The fitted asymmetry is corrected

for charge confusion, which is estimated from the data to be $(7 \pm 3)\%$ for a single tau. The asymmetries are corrected for backgrounds from other final states. For high energy events, the correction includes the effect of the contamination from events with hard ISR photons.

Table 3 summarises the number of forward and backward events, the background correction, and the corrected asymmetries. In Figure 5 the comparison of the measured asymmetries to the Standard Model prediction is shown.

3.4 $e^+e^- \rightarrow e^+e^-(\gamma)$

Event Selection

The selection used in [2] is modified to include events with hard ISR photons. The energy, E_{max} , of the highest energy cluster in the electromagnetic calorimeter is required to be larger than 60% of the beam energy. The acollinearity angle between the two highest energy clusters has to be less than 60 degrees. To reject events from the reaction $e^+e^- \rightarrow \gamma\gamma(\gamma)$ a track in the central tracking chamber matched with a cluster in the electromagnetic calorimeter is required. The t -channel contribution from Bhabha scattering is reduced by restricting the polar angle of both leptons to $44^\circ < \theta < 136^\circ$.

The $\sqrt{s'}$ value is reconstructed from the invariant mass of the two highest energy clusters in the electromagnetic calorimeter. Its distribution is shown in Figure 6a. A cut of 110 GeV isolates high energy events.

Cross Section

The selection efficiencies within the fiducial volume and the background contributions are listed in Table 1. The total systematic error of 2% assigned to the cross section measurements is dominated by uncertainties in the event selection. An alternative selection, differing in the rejection of $e^+e^- \rightarrow \gamma\gamma(\gamma)$ events, yields consistent results.

Table 2 summarises the number of selected events and the resulting cross sections for the two event samples at the different centre-of-mass energies. The results are given for $44^\circ < \theta < 136^\circ$ and an acollinearity angle cut of 60 degrees. The cross sections are compared to the Standard Model prediction in Figure 7.

By requiring the absence of tracks in the central tracking chamber the cross section of the reaction $e^+e^- \rightarrow \gamma\gamma(\gamma)$ is measured. The results are listed in Table 4. The measurements agree well with the QED prediction.

Forward-Backward Asymmetry

The electron direction in the event is determined by a two-dimensional method [2] based on angular and momentum information from the central tracking chamber and the silicon microstrip detector. The probability of a wrong charge assignment is determined using the momentum and angular resolutions as obtained from data. It is found to be $(7 \pm 2)\%$ for the total and $(6 \pm 2)\%$ for the high energy event sample, and its uncertainty is the dominant contribution to the systematic error.

The differential cross section for the high energy event sample at 136 GeV is shown in Figure 6b. The effect of t -channel photon exchange producing predominantly forward events is clearly visible.

The forward–backward asymmetry is measured by counting events in the forward and backward hemispheres. Table 3 summarises the number of forward and backward events, the charge correction, and the corrected asymmetries. The systematic error of the measured asymmetry is estimated to be 0.034 for the total and 0.037 for the high energy event sample. In Figure 7 the comparison of the measured asymmetries to the Standard Model prediction is shown.

3.5 $e^+e^- \rightarrow \nu\bar{\nu}\gamma(\gamma)$

Event Selection

Radiative neutrino–pair production, $e^+e^- \rightarrow \nu\bar{\nu}\gamma(\gamma)$, is tagged by ISR photons. The photons are detected in the barrel part, $45^\circ < \theta_\gamma < 135^\circ$, and the endcap parts, $20^\circ < \theta_\gamma < 35^\circ$ and $145^\circ < \theta_\gamma < 160^\circ$, of the electromagnetic calorimeter. They are identified as calorimetric clusters with electromagnetic shower shape, an energy larger than 1 GeV in the barrel or 10 GeV in the endcaps, and no track in the central tracking chamber. The energies of the highest energy clusters in the luminosity monitor, the low–angle lead–scintillator calorimeter, and the hadronic calorimeter must all be smaller than 5 GeV. Contamination arising from cosmic ray muons with bremsstrahlung is suppressed by removing events with reconstructed tracks in the muon chambers.

Cross Section

After these cuts, 40 events are found, with an expected background from $e^+e^- \rightarrow \gamma\gamma(\gamma)$ and $e^+e^- \rightarrow e^+e^-(\gamma)$ of 13 events. The energy distribution of these events together with the Monte Carlo expectation is shown in Figure 8. The distribution peaks at about 35 GeV, showing the photon energy due to the radiative return to the Z. To fully suppress the background of radiative Bhabha events only photons with an energy above 3 GeV are used to measure the cross section. The cosmic ray background in the final event sample is estimated to be less than 1%.

The trigger efficiency is measured to be $(81.2 \pm 1.4)\%$ for photons up to 8 GeV in the barrel. It rises to $(97.7 \pm 2.3)\%$ for photons above 10 GeV in barrel and endcaps. These efficiencies are determined from radiative Bhabha events as described in [24]. Cross sections are determined for events with at least one photon above 3 GeV and $20^\circ < \theta_\gamma < 160^\circ$, and for the full phase space. The total efficiency for the $\nu\bar{\nu}\gamma(\gamma)$ final state is determined to be $(56 \pm 3)\%$ for the restricted and $(6.5 \pm 0.4)\%$ for the full phase space. A systematic error on the cross section measurements of 5% is derived.

Table 5 summarises the number of selected events and the resulting cross sections for the two different centre–of–mass energies together with the Standard Model prediction.

To allow the interpretation of the results for single–photon processes with different spectra the efficiencies for photon detection including the trigger are given: $(75 \pm 3)\%$ for photons with an energy from 3 GeV to 8 GeV in the barrel, and $(90 \pm 3)\%$ for photons with an energy larger than 10 GeV in barrel and endcaps.

4 Interpretation of the Results

Our data are interpreted in the framework of the S–Matrix ansatz [3], which makes a minimum of theoretical assumptions. This ansatz describes the hard scattering process of fermion–pair production in e^+e^- annihilations by the s –channel exchange of two spin–1 bosons, a massless

photon and a massive Z boson. The lowest-order total cross section, σ_{tot}^0 , and forward-backward asymmetry, A_{fb}^0 , for $e^+e^- \rightarrow f\bar{f}$ are given as [3,25]:

$$\sigma_a^0(s) = \frac{4}{3}\pi\alpha^2 \left[\frac{g_f^a}{s} + \frac{s r_f^a + (s - \bar{m}_Z^2) j_f^a}{(s - \bar{m}_Z^2)^2 + \bar{m}_Z^2 \bar{\Gamma}_Z^2} \right] \quad \text{for } a = \text{tot, fb}$$

$$A_{\text{fb}}^0(s) = \frac{3}{4} \frac{\sigma_{\text{fb}}^0(s)}{\sigma_{\text{tot}}^0(s)}.$$

The S-Matrix ansatz is defined using a Breit-Wigner denominator with s -independent width for the Z resonance. To derive the mass and width of the Z boson for a Breit-Wigner with s -dependent width, the following transformations are applied [3]: $m_Z = \bar{m}_Z + 34 \text{ MeV}$ and $\Gamma_Z = \bar{\Gamma}_Z + 1 \text{ MeV}$.

The S-Matrix parameters r_f , j_f and g_f scale the Z exchange, γZ interference and γ exchange contributions. In our approach, the γ exchange contributions g_f are fixed by QED, $g_f^{\text{tot}} = q_e^2 q_f^2$ and $g_f^{\text{fb}} = 0$, where q_f is the electric charge of the fermion f . QED radiative corrections are included by convolution with a radiator function [26].

The program SMATASY [25] together with ZFITTER [19] and ALIBABA [20] is used for the calculation of the theoretical predictions of cross sections and forward-backward asymmetries. The S-Matrix parameters are determined in a χ^2 fit to the measurements presented here and to our previously published Z measurements [2]. The uncertainty on the LEP centre-of-mass energy of 70 MeV for the high energy measurements [27] has a negligible effect on the fit results.

The errors on the γZ interference parameters are reduced when fitting the measurements with a $\sqrt{s'}$ cut applied. The fitted S-Matrix parameters for electrons, muons, taus and hadrons, and their correlations, are listed in Tables 6 and 7. The fits are performed with and without the assumption of lepton universality. The parameters obtained for the individual leptons are in agreement with each other and support this assumption.

A large correlation between the mass of the Z boson and the hadronic γZ interference term, $j_{\text{had}}^{\text{tot}}$, is found. This correlation causes an increase in the error on m_Z with respect to fits where the hadronic γZ interference term is fixed to its Standard Model prediction [2,4,28]. The fitted hadronic γZ interference term is:

$$j_{\text{had}}^{\text{tot}} = 0.29 \pm 0.41,$$

which agrees well with the Standard Model prediction of 0.22 and improves on the accuracy of our previous result [4] by almost a factor of 2. The fitted value for m_Z ,

$$m_Z = 91196 \pm 9 \pm 6 \text{ MeV},$$

where the second error arises from the γZ interference contributions, agrees well with our previous result. The total error on m_Z in a fit with free γZ interference terms improves from 14 MeV to 11 MeV. This decrease arises from the reduction in the error component caused by the γZ interference terms from 11 MeV to 6 MeV. Figure 9 shows the correlation contours between m_Z and $j_{\text{had}}^{\text{tot}}$ under the assumption of lepton universality.

5 Summary and Conclusion

Based on an integrated luminosity of 5 pb^{-1} collected at centre-of-mass energies between 130 GeV and 140 GeV, we select 1577 hadronic and 401 lepton-pair events. The data are used

to perform the first measurements of cross sections and leptonic forward–backward asymmetries at these centre–of–mass energies. All measurements are well described by the Standard Model.

Our measurements allow an improved determination of the γZ interference terms and improve the accuracy of the Z mass determined within the S–Matrix framework.

Acknowledgements

We wish to congratulate the CERN accelerator divisions for the successful upgrade of the LEP machine and to express our gratitude for the excellent performance of the machine. We acknowledge with appreciation the effort of all engineers, technicians and support staff who have participated in the construction and maintenance of this experiment. Those of us who are not from member states thank CERN for its hospitality and help.

References

- [1] S. L. Glashow, Nucl. Phys. **22** (1961) 579;
S. Weinberg, Phys. Rev. Lett. **19** (1967) 1264;
A. Salam, “Elementary Particle Theory”, ed. N. Svartholm, Stockholm, “Almqvist and Wiksell” (1968), 367.
- [2] L3 Collab., M. Acciarri *et al.*, Z. Phys. **C 62** (1994) 551.
- [3] A. Leike, T. Riemann and J. Rose, Phys. Lett. **B 273** (1991) 513;
T. Riemann, Phys. Lett. **B 293** (1992) 451.
- [4] L3 Collab., O. Adriani *et al.*, Phys. Lett. **B 315** (1993) 494.
- [5] L3 Collab., B. Adeva *et al.*, Nucl. Inst. Meth. **A 289** (1990) 35.
- [6] M. Acciarri *et al.*, Nucl. Inst. Meth. **A 351** (1994) 300.
- [7] M. Chemarin *et al.*, Nucl. Inst. Meth. **A 349** (1994) 345.
- [8] A. Adam *et al.*, “The Forward Muon Detector of L3”,
to be published in Nucl. Inst. Meth.
- [9] M. Merk, Proceedings of the XXIXth Rencontre de Moriond, Meribel les Allues, France –
March 12–19, 1994, ed. J. Tran Thanh Van.
- [10] The L3 detector simulation is based on GEANT Version 3.15.
R. Brun *et al.*, “GEANT 3”, CERN-DD/EE/84-1 (Revised), 1987.
The GHEISHA program (H. Fesefeldt, RWTH Aachen Report PITHA 85/02 (1985))
is used to simulate hadronic interactions.
- [11] The BHLUMI version 4.03 is used.
S. Jadach *et al.*, Comp. Phys. Comm. **70** (1992) 305;
S. Jadach *et al.*, Phys. Lett. **B 353** (1995) 349;
S. Jadach *et al.*, Phys. Lett. **B 353** (1995) 362.
- [12] S. Jadach *et al.*, Proceedings of the CERN Workshop on Physics at LEP-2;
S. Jadach, private communication.
- [13] T. Sjöstrand, “PYTHIA 5.7 and JETSET 7.4 Physics and Manual”,
CERN-TH/7112/93 (1993), revised August 1995;
T. Sjöstrand, Comp. Phys. Comm. **82** (1994) 74.
- [14] The KORALZ version 4.01 is used.
S. Jadach, B. F. L. Ward and Z. Wąs, Comp. Phys. Comm. **79** (1994) 503.
- [15] J. H. Field, Phys. Lett. **B 323** (1994) 432;
J. H. Field and T. Riemann, Preprints UGVA-DPNC 1995/6-166 and DESY 95-100,
to be published in Comp. Phys. Comm.
- [16] R. Miquel *et al.*, Z. Phys. **C 48** (1990) 309;
F. A. Berends *et al.*, Nucl. Phys. **B 301** (1988) 583.

- [17] F. A. Berends, P. H. Daverfeldt and R. Kleiss, Nucl. Phys. **B 253** (1985) 441.
- [18] F. A. Berends and R. Kleiss, Nucl. Phys. **B 186** (1981) 22.
- [19] D. Bardin *et al.*, FORTRAN package ZFITTER 4.9, and Preprint CERN–TH/6443/92;
D. Bardin *et al.*, Z. Phys. **C 44** (1989) 493;
D. Bardin *et al.*, Nucl. Phys. **B 351** (1991) 1;
D. Bardin *et al.*, Phys. Lett. **B 255** (1991) 290.
- [20] W. Beenakker, F. Berends and S. van der Marck, Nucl. Phys. **B 349** (1991) 323.
- [21] L3 Collab., O. Adriani *et al.*, Physics Reports **236** (1993) 1.
- [22] CDF Collab., F. Abe *et al.*, Phys. Rev. Lett. **74** (1995) 2626;
D0 Collab., S. Abachi *et al.*, Phys. Rev. Lett. **74** (1995) 2632.
- [23] S. Eidelman and F. Jegerlehner, Z. Phys. **C 67** (1995) 585.
- [24] L3 Collab., O. Adriani *et al.*, Phys. Lett. **B 292** (1992) 463;
L3 Collab., O. Adriani *et al.*, Phys. Lett. **B 297** (1992) 469.
- [25] The SMATASY version 4.9 is used.
S. Kirsch and T. Riemann, Comp. Phys. Comm. **88** (1995) 89.
- [26] F. A. Berends *et al.*, in “Z Physics at LEP 1”, Report CERN 89–08 (1989),
eds G. Altarelli, R. Kleiss and C. Verzegnassi, Vol. 1, p. 89;
M. Böhm *et al.*, *ibid*, p. 203.
- [27] The LEP Energy Working Group, private communication.
- [28] G. Isidori, Phys. Lett. **B 314** (1993) 139;
M. Grünewald and S. Kirsch, Preprint CERN–PPE/93–188 (1993).

The L3 Collaboration:

M.Acciarri,²⁹ A.Adam,⁴⁸ O.Adriani,¹⁸ M.Aguilar-Benitez,²⁸ S.Ahlen,¹² B.Alpat,³⁶ J.Alcaraz,²⁸ J.Allaby,¹⁹ A.Aloisio,³¹ G.Alverson,¹³ M.G.Alvigi,³¹ G.Ambrosi,³⁶ H.Anderhub,⁵¹ V.P.Andreev,⁴⁰ T.Angelescu,⁴ D.Antreasyan,¹⁰ A.Arefiev,³⁰ T.Azmoon,³ T.Aziz,¹¹ P.Bagnaia,^{39,19} L.Baksay,⁴⁶ R.C.Ball,³ S.Banerjee,¹¹ K.Banicz,⁴⁸ R.Barillère,¹⁹ L.Barone,³⁹ P.Bartalini,³⁶ A.Baschirotto,²⁹ M.Basile,¹⁰ R.Battiston,³⁶ A.Bay,²⁴ F.Becattini,⁸ U.Becker,¹⁷ F.Behner,⁵¹ Gy.L.Bencze,¹⁵ J.Berdugo,²⁸ P.Berges,¹⁷ B.Bertucci,¹⁹ B.L.Betev,⁵¹ M.Biasini,¹⁹ A.Biland,⁵¹ G.M.Bilei,³⁶ J.J.Blaising,¹⁹ S.C.Blyth,³⁷ G.J.Bobbink,² R.Bock,¹ A.Böhm,¹ B.Borgia,³⁹ A.Boucham,⁴ D.Bourilkov,⁵¹ M.Bourquin,²¹ D.Boutigny,⁴ E.Brambilla,¹⁷ J.G.Branson,⁴² V.Brigljevic,⁵¹ I.C.Brock,³⁷ A.Buijs,⁴⁷ A.Bujak,⁴⁸ J.D.Burger,¹⁷ W.J.Burger,²¹ C.Burgos,²⁸ J.Busenitz,⁴⁶ A.Buytenhuijs,³³ X.D.Cai,²⁰ M.Campanelli,⁵¹ M.Capell,¹⁷ G.Cara Romeo,¹⁰ M.Caria,³⁶ G.Carlini,⁴ A.M.Cartacci,¹⁸ J.Casaus,²⁸ G.Castellini,¹⁸ R.Castello,⁹ F.Cavallari,³⁹ N.Cavallo,³¹ C.Cecchi,²¹ M.Cerrada,²⁸ F.Cesaroni,²⁵ M.Chamizo,²⁸ A.Chan,⁵³ Y.H.Chang,⁵³ U.K.Chaturvedi,²⁰ M.Chemarin,²⁷ A.Chen,⁵³ C.Chen,⁸ G.Chen,⁸ G.M.Chen,⁸ H.F.Chen,²² H.S.Chen,⁸ X.Chereau,⁴ G.Chiefari,³¹ C.Y.Chien,⁵ M.T.Choi,⁴⁵ L.Cifarelli,⁴¹ F.Cindolo,¹⁰ C.Civini,¹⁸ I.Clare,¹⁷ R.Clare,¹⁷ T.E.Coan,²⁶ H.O.Cohn,³⁴ G.Coignet,⁴ A.P.Colijn,² N.Colino,²⁸ V.Commichau,³ S.Costantini,³⁹ F.Cotorobai,⁴ B.de la Cruz,²⁸ T.S.Dai,⁷ R.D'Alessandro,¹⁸ R.de Asmundis,³¹ H.De Boeck,³³ A.Degré,⁴ K.Deiters,⁴⁹ E.Dénes,¹⁵ P.Denes,³⁸ F.DeNotaristefani,³⁹ D.DiBitonto,⁴⁶ M.Diemoz,³⁹ D.van Dierendonck,² F.Di Lodovico,⁵¹ C.Dionisi,³⁹ M.Dittmar,⁵¹ A.Dominguez,⁴² A.Doria,³¹ I.Dorne,⁴ M.T.Dova,^{20,†} E.Drago,³¹ D.Duchesneau,⁴ P.Duinker,² I.Duran,⁴³ S.Dutta,¹¹ S.Easo,³⁶ Yu.Efremenko,³⁴ H.El Mamouni,²⁷ A.Engler,³⁷ F.J.Eppling,¹⁷ F.C.Erné,² J.P.Ernenwein,²⁷ P.Extermann,²¹ R.Fabbretti,⁴⁹ M.Fabre,⁴⁹ R.Faccini,³⁹ S.Falciano,³⁹ A.Favara,⁸ J.Fay,²⁷ M.Felcini,⁵¹ T.Ferguson,³⁷ D.Fernandez,²⁸ G.Fernandez,²⁸ F.Ferroni,³⁹ H.Fesefeldt,¹ E.Fiandrini,³⁶ J.H.Field,²¹ F.Filthaut,³⁷ P.H.Fisher,¹⁷ G.Forconi,¹⁷ L.Fredj,²¹ K.Freudenreich,⁵¹ M.Gailloud,²⁴ Yu.Galaktionov,^{30,17} S.N.Ganguli,¹¹ P.Garcia-Abia,²⁸ S.S.Gau,¹³ S.Gentile,³⁹ J.Gerald,⁵ N.Gheordanescu,¹⁴ S.Giagu,³⁹ S.Goldfarb,²⁴ J.Goldstein,¹² Z.F.Gong,²² E.Gonzalez,²⁸ A.Gougas,⁵ D.Goujon,²¹ G.Gratta,³⁵ M.W.Gruenewald,⁹ V.K.Gupta,³⁸ A.Gurtu,¹¹ H.R.Gustafson,³ L.J.Gutay,⁴⁸ K.Hangarter,¹ B.Hartmann,¹ A.Hasan,³² J.T.He,⁸ T.Hebbeker,⁹ A.Hervé,¹⁹ W.C.van Hoek,³³ H.Hofer,⁵¹ H.Hoorani,²¹ S.R.Hou,⁵³ G.Hu,²⁰ M.M.Ilyas,²⁰ V.Innocente,¹⁹ H.Janssen,⁴ B.N.Jin,⁸ L.W.Jones,³ P.de Jong,¹⁷ I.Josa-Mutuberria,²⁸ A.Kasser,²⁴ R.A.Khan,²⁰ Yu.Kamyshkov,³⁴ P.Kapinos,⁵⁰ J.S.Kapustinsky,²⁶ Y.Karyotakis,⁴ M.Kaur,^{20,◇} M.N.Kienzle-Focacci,²¹ D.Kim,⁵ J.K.Kim,⁴⁵ S.C.Kim,⁴⁵ Y.G.Kim,⁴⁵ W.W.Kinnison,²⁶ A.Kirkby,³⁵ D.Kirkby,³⁵ J.Kirkby,¹⁹ W.Kittel,³³ A.Klimentov,^{17,30} A.C.König,³³ E.Koffeman,² A.Königter,¹ V.Koutsenko,^{17,30} A.Koulbardi,⁴⁰ R.W.Kraemer,³⁷ T.Kramer,¹⁷ W.Krenz,¹ H.Kuijten,³³ A.Kunin,^{17,30} P.Ladron de Guevara,²⁸ G.Landi,¹⁸ C.Lapoint,¹⁷ K.Lassila-Perini,⁵¹ P.Laurikainen,²³ M.Lebeau,¹⁹ A.Lebedev,¹⁷ P.Lebrun,²⁷ P.Lecomte,⁵¹ P.Lecoq,¹⁹ P.Le Coultre,⁵¹ J.S.Lee,⁴⁵ K.Y.Lee,⁴⁵ C.Leggett,³ J.M.Le Goff,¹⁹ R.Leiste,⁵⁰ M.Lenti,¹⁸ E.Leonardi,³⁹ P.Levtchenko,⁴⁰ C.Li,²² E.Lieb,⁵⁰ W.T.Lin,⁵³ F.L.Linde,² B.Lindemann,¹ L.Lista,³¹ Z.A.Liu,⁸ W.Lohmann,⁵⁰ E.Longo,³⁹ W.Lu,³⁵ Y.S.Lu,⁸ K.Lübelsmeyer,¹ C.Luci,³⁹ D.Luckey,¹⁷ L.Ludovici,³⁹ L.Luminari,³⁹ W.Lustermann,⁴⁹ W.G.Ma,²² A.Macchiolo,⁸ M.Maity,¹¹ G.Majumder,¹¹ L.Malgeri,³⁹ A.Malinin,³⁰ C.Maña,²⁸ S.Mangla,¹¹ M.Maolinbay,⁵¹ P.Marchesini,⁵¹ A.Marin,¹² J.P.Martin,²⁷ F.Marzano,³⁹ G.G.G.Massarò,² K.Mazumdar,¹¹ D.McNally,¹⁹ R.R.McNeil,⁷ S.Mele,³¹ L.Merola,³¹ M.Meschini,¹⁸ W.J.Metzger,³³ M.von der Mey,¹ Y.Mi,²⁴ A.Mihul,⁴ A.J.W.van Mil,³³ G.Mirabelli,³⁹ J.Mnich,¹⁹ M.Möller,¹ B.Montealeoni,¹⁸ R.Moore,³ S.Morganti,³⁹ R.Mount,³⁵ S.Müller,¹ F.Muheim,²¹ E.Nagy,¹⁵ S.Nahn,¹⁷ M.Napolitano,³¹ F.Nessi-Tedaldi,⁵¹ H.Newman,³⁵ A.Nippe,¹ H.Nowak,⁵⁰ G.Organtini,³⁹ R.Ostonen,²³ D.Pandoulas,¹ S.Paoletti,³¹ P.Paolucci,³¹ H.K.Park,³⁷ G.Pascale,³⁹ G.Passaleva,¹⁸ S.Patricelli,³¹ T.Paul,³⁶ M.Pauluzzi,³⁶ C.Paus,⁵¹ F.Pauss,⁵¹ Y.J.Pei,¹ S.Pensotti,²⁹ D.Perret-Gallix,⁴ S.Petrak,⁹ A.Pevsner,⁵ D.Piccolo,³¹ M.Pieri,¹⁸ J.C.Pinto,³⁷ P.A.Piroué,³⁸ E.Pistolesi,¹⁸ V.Plyaskin,³⁰ M.Pohl,⁵¹ V.Pojidaev,^{30,18} H.Postema,¹⁷ N.Produit,²¹ R.Raghavan,¹¹ G.Rahal-Callot,⁵¹ P.G.Rancoita,²⁹ M.Rattaggi,²⁹ G.Raven,⁴² P.Razis,³² K.Read,³⁴ M.Redaeli,²⁹ D.Ren,⁵¹ M.Rescigno,³⁹ S.Reucroft,¹³ A.Ricker,¹ S.Riemann,⁵⁰ B.C.Riemers,⁴⁸ K.Riles,³ O.Rind,³ S.Ro,⁴⁵ A.Robohm,⁵¹ J.Rodin,¹⁷ F.J.Rodriguez,²⁸ B.P.Roe,³ S.Röhner,¹ L.Romero,²⁸ S.Rosier-Lees,⁴ Ph.Rossetet,²⁴ W.van Rossum,⁴⁷ S.Roth,¹ J.A.Rubio,¹⁹ H.Rykaczewski,⁵¹ J.Salicio,¹⁹ J.M.Salicio,²⁸ E.Sanchez,²⁸ A.Santocchia,³⁶ M.E.Sarakinos,²³ S.Sarkar,¹¹ M.Sassowsky,¹ C.Schäfer,¹ V.Schegelsky,⁴⁰ S.Schmidt-Kaerst,¹ D.Schmitz,¹ P.Schmitz,¹ M.Schneegans,⁴ B.Schoenich,⁵⁰ N.Scholz,⁵¹ H.Schopper,⁵² D.J.Schotanus,³³ R.Schulte,¹ K.Schultze,¹ J.Schwenke,¹ G.Schwering,¹ C.Sciacca,³¹ P.G.Seiler,⁴⁹ J.C.Sens,⁵³ L.Servoli,³⁶ S.Shevchenko,³⁵ N.Shivarov,⁴⁴ V.Shoutko,³⁰ J.Shukla,²⁶ E.Shumilov,³⁰ T.Siedenbun,¹ D.Son,⁴⁵ A.Sopczak,⁵⁰ V.Soulimov,³¹ B.Smith,¹⁷ P.Spillantini,¹⁸ M.Steuer,¹⁷ D.P.Stickland,³⁸ F.Sticozzi,¹⁷ H.Stone,³⁸ B.Stoyanov,⁴⁴ A.Straessner,¹ K.Strauch,¹⁶ K.Sudhakar,¹¹ G.Sultanov,²⁰ L.Z.Sun,²² G.F.Susinno,²¹ H.Suter,⁵¹ J.D.Swain,²⁰ X.W.Tang,⁸ L.Tauscher,⁶ L.Taylor,¹³ Samuel C.C.Ting,¹⁷ S.M.Ting,¹⁷ O.Toker,³⁶ F.Tonisch,⁵⁰ M.Tonutti,¹ S.C.Tonwar,¹¹ J.Tóth,¹⁵ A.Tsaregorodtsev,⁴⁰ C.Tully,³⁸ H.Tuchscherer,⁴⁶ K.L.Tung,⁸ J.Ulbricht,⁵¹ L.Urbán,¹⁵ U.Uwer,¹⁹ E.Valente,³⁹ R.T.Van de Walle,³³ I.Vetlitsky,³⁰ G.Viertel,⁵¹ M.Vivargent,⁴ R.Völkert,⁵⁰ H.Vogel,³⁷ H.Vogt,⁵⁰ I.Vorobiev,³⁰ A.A.Vorobyov,⁴⁰ An.A.Vorobyov,⁴⁰ L.Vuilleumier,²⁴ M.Wadhwa,⁶ W.Wallraff,¹ J.C.Wang,¹⁷ X.L.Wang,²² Y.F.Wang,¹⁷ Z.M.Wang,²² A.Weber,¹ R.Weill,²⁴ C.Willmott,²⁸ F.Wittgenstein,¹⁹ S.X.Wu,²⁰ S.Wynhoff,¹ J.Xu,¹² Z.Z.Xu,²² B.Z.Yang,²² C.G.Yang,⁸ X.Y.Yao,⁸ J.B.Ye,²² S.C.Yeh,⁵³ J.M.You,³⁷ C.Zaccardelli,³⁵ An.Zalite,⁴⁰ P.Zemp,⁵¹ J.Y.Zeng,⁸ Y.Zeng,¹ Z.Zhang,⁸ Z.P.Zhang,²² B.Zhou,¹² G.J.Zhou,⁸ Y.Zhou,³ G.Y.Zhu,⁸ R.Y.Zhu,³⁵ A.Zichichi,^{10,19,20} B.C.C.van der Zwaan,²

- 1 I. Physikalisches Institut, RWTH, D-52056 Aachen, FRG[§]
 - III. Physikalisches Institut, RWTH, D-52056 Aachen, FRG[§]
 - 2 National Institute for High Energy Physics, NIKHEF, and University of Amsterdam, NL-1009 DB Amsterdam, The Netherlands
 - 3 University of Michigan, Ann Arbor, MI 48109, USA
 - 4 Laboratoire d'Annecy-le-Vieux de Physique des Particules, LAPP,IN2P3-CNRS, BP 110, F-74941 Annecy-le-Vieux CEDEX, France
 - 5 Johns Hopkins University, Baltimore, MD 21218, USA
 - 6 Institute of Physics, University of Basel, CH-4056 Basel, Switzerland
 - 7 Louisiana State University, Baton Rouge, LA 70803, USA
 - 8 Institute of High Energy Physics, IHEP, 100039 Beijing, China
 - 9 Humboldt University, D-10099 Berlin, FRG[§]
 - 10 INFN-Sezione di Bologna, I-40126 Bologna, Italy
 - 11 Tata Institute of Fundamental Research, Bombay 400 005, India
 - 12 Boston University, Boston, MA 02215, USA
 - 13 Northeastern University, Boston, MA 02115, USA
 - 14 Institute of Atomic Physics and University of Bucharest, R-76900 Bucharest, Romania
 - 15 Central Research Institute for Physics of the Hungarian Academy of Sciences, H-1525 Budapest 114, Hungary[‡]
 - 16 Harvard University, Cambridge, MA 02139, USA
 - 17 Massachusetts Institute of Technology, Cambridge, MA 02139, USA
 - 18 INFN Sezione di Firenze and University of Florence, I-50125 Florence, Italy
 - 19 European Laboratory for Particle Physics, CERN, CH-1211 Geneva 23, Switzerland
 - 20 World Laboratory, FBLJA Project, CH-1211 Geneva 23, Switzerland
 - 21 University of Geneva, CH-1211 Geneva 4, Switzerland
 - 22 Chinese University of Science and Technology, USTC, Hefei, Anhui 230 029, China
 - 23 SEFT, Research Institute for High Energy Physics, P.O. Box 9, SF-00014 Helsinki, Finland
 - 24 University of Lausanne, CH-1015 Lausanne, Switzerland
 - 25 INFN-Sezione di Lecce and Università Degli Studi di Lecce, I-73100 Lecce, Italy
 - 26 Los Alamos National Laboratory, Los Alamos, NM 87544, USA
 - 27 Institut de Physique Nucléaire de Lyon, IN2P3-CNRS, Université Claude Bernard, F-69622 Villeurbanne, France
 - 28 Centro de Investigaciones Energeticas, Medioambientales y Tecnológicas, CIEMAT, E-28040 Madrid, Spain[‡]
 - 29 INFN-Sezione di Milano, I-20133 Milan, Italy
 - 30 Institute of Theoretical and Experimental Physics, ITEP, Moscow, Russia
 - 31 INFN-Sezione di Napoli and University of Naples, I-80125 Naples, Italy
 - 32 Department of Natural Sciences, University of Cyprus, Nicosia, Cyprus
 - 33 University of Nymegen and NIKHEF, NL-6525 ED Nymegen, The Netherlands
 - 34 Oak Ridge National Laboratory, Oak Ridge, TN 37831, USA
 - 35 California Institute of Technology, Pasadena, CA 91125, USA
 - 36 INFN-Sezione di Perugia and Università Degli Studi di Perugia, I-06100 Perugia, Italy
 - 37 Carnegie Mellon University, Pittsburgh, PA 15213, USA
 - 38 Princeton University, Princeton, NJ 08544, USA
 - 39 INFN-Sezione di Roma and University of Rome, "La Sapienza", I-00185 Rome, Italy
 - 40 Nuclear Physics Institute, St. Petersburg, Russia
 - 41 University and INFN, Salerno, I-84100 Salerno, Italy
 - 42 University of California, San Diego, CA 92093, USA
 - 43 Dept. de Física de Partículas Elementales, Univ. de Santiago, E-15706 Santiago de Compostela, Spain
 - 44 Bulgarian Academy of Sciences, Central Laboratory of Mechatronics and Instrumentation, BU-1113 Sofia, Bulgaria
 - 45 Center for High Energy Physics, Korea Advanced Inst. of Sciences and Technology, 305-701 Taejon, Republic of Korea
 - 46 University of Alabama, Tuscaloosa, AL 35486, USA
 - 47 Utrecht University and NIKHEF, NL-3584 CB Utrecht, The Netherlands
 - 48 Purdue University, West Lafayette, IN 47907, USA
 - 49 Paul Scherrer Institut, PSI, CH-5232 Villigen, Switzerland
 - 50 DESY-Institut für Hochenergiephysik, D-15738 Zeuthen, FRG
 - 51 Eidgenössische Technische Hochschule, ETH Zürich, CH-8093 Zürich, Switzerland
 - 52 University of Hamburg, D-22761 Hamburg, FRG
 - 53 High Energy Physics Group, Taiwan, China
- [§] Supported by the German Bundesministerium für Bildung, Wissenschaft, Forschung und Technologie
[‡] Supported by the Hungarian OTKA fund under contract numbers 2970 and T14459.
[‡] Supported also by the Comisión Interministerial de Ciencia y Tecnología
[‡] Also supported by CONICET and Universidad Nacional de La Plata, CC 67, 1900 La Plata, Argentina
[◇] Also supported by Panjab University, Chandigarh-160014, India

	total [%]	high energy [%]
$e^+e^- \rightarrow \text{hadrons}(\gamma)$		
Selection Efficiency	95.5 ± 1.1	99.3 ± 0.2
Background	2.3 ± 0.3	2.7 ± 0.4
Fit Systematics	—	1.3
Total Systematics	1.1	1.5
$e^+e^- \rightarrow \mu^+\mu^-(\gamma)$		
Selection Efficiency	$60.8 (59.1) \pm 0.7 (0.7)$	70.3 ± 1.1
Cosmic Background	$3.8 (6.1) \pm 1.5 (2.1)$	$5.8 (7.7) \pm 3.2 (3.8)$
Other Background	6.0 ± 0.9	3.8 ± 1.0
ISR Contamination	—	$12.9 (12.5) \pm 0.9 (0.9)$
Detector Systematics	3	3
Total Systematics	4	5
$e^+e^- \rightarrow \tau^+\tau^-(\gamma)$		
Selection Efficiency	42.9 ± 0.5	$50.9 (53.4) \pm 0.8 (0.8)$
Background	10.0 ± 1.9	11.5 ± 3.3
ISR Contamination	—	$15.0 (14.0) \pm 1.0 (1.0)$
Cut Variation	5	5
Total Systematics	5	6
$e^+e^- \rightarrow e^+e^-(\gamma)$		
Selection Efficiency	98.5 ± 0.1	95.3 ± 0.1
Background	2.7 ± 0.3	0.8 ± 0.2
ISR Contamination	—	0.5 ± 0.1
Cut Variation	2	2
Total Systematics	2	2

Table 1: Efficiencies, backgrounds and systematic uncertainties for the total and the high energy, $\sqrt{s'} > 110$ GeV, event samples of the reactions $e^+e^- \rightarrow \text{hadrons}(\gamma)$, $e^+e^- \rightarrow \mu^+\mu^-(\gamma)$, $e^+e^- \rightarrow \tau^+\tau^-(\gamma)$ and $e^+e^- \rightarrow e^+e^-(\gamma)$. For the electron pair production the efficiencies are given for $44^\circ < \theta < 136^\circ$ and an acollinearity angle cut of $\xi < 60^\circ$. When differences are observed as a function of \sqrt{s} the numbers for 130 (136) GeV are given separately.

		total		high energy	
$e^+e^- \rightarrow \text{hadrons}(\gamma)$					
\sqrt{s} [GeV]	\mathcal{L} [pb ⁻¹]	N_{events}	σ_{had} [pb]	N_{events}	σ_{had} [pb]
130.3	2.74	921	343 ± 11	263	81.8 ± 6.4
136.3	2.25	645	293 ± 12	202	70.5 ± 6.2
140.2	0.05	11	235 ± 71	4	67 ± 47
$e^+e^- \rightarrow \mu^+\mu^-(\gamma)$					
\sqrt{s} [GeV]	\mathcal{L} [pb ⁻¹]	N_{events}	$\sigma_{\mu^+\mu^-}$ [pb]	N_{events}	$\sigma_{\mu^+\mu^-}$ [pb]
130.3	2.74	47	25.5 ± 3.7	19	7.7 ± 1.8
136.3	2.30	28	18.1 ± 3.3	13	6.1 ± 1.7
$e^+e^- \rightarrow \tau^+\tau^-(\gamma)$					
\sqrt{s} [GeV]	\mathcal{L} [pb ⁻¹]	N_{events}	$\sigma_{\tau^+\tau^-}$ [pb]	N_{events}	$\sigma_{\tau^+\tau^-}$ [pb]
130.3	2.54	31	25.5 ± 4.8	15	10.4 ± 2.8
136.3	2.25	22	20.3 ± 4.6	13	9.4 ± 2.8
$e^+e^- \rightarrow e^+e^-(\gamma)$					
\sqrt{s} [GeV]	\mathcal{L} [pb ⁻¹]	N_{events}	$\sigma_{e^+e^-}$ [pb]	N_{events}	$\sigma_{e^+e^-}$ [pb]
130.3	2.68	136	50.1 ± 4.4	113	43.7 ± 4.1
136.3	2.29	110	47.8 ± 4.6	95	43.2 ± 4.5

Table 2: Number of selected events and cross sections of the reactions $e^+e^- \rightarrow \text{hadrons}(\gamma)$, $e^+e^- \rightarrow \mu^+\mu^-(\gamma)$, $e^+e^- \rightarrow \tau^+\tau^-(\gamma)$ and $e^+e^- \rightarrow e^+e^-(\gamma)$ for the total and the high energy, $\sqrt{s'} > 110$ GeV, event samples. For the electron pair production the cross sections are given for $44^\circ < \theta < 136^\circ$ and an acollinearity angle cut of $\xi < 60^\circ$.

$e^+e^- \rightarrow \mu^+\mu^-(\gamma)$								
	total				high energy			
\sqrt{s} [GeV]	N_f	N_b	c	A_{fb}	N_f	N_b	c	A_{fb}
130.3	30	17	1.11 ± 0.02	$0.30_{-0.15}^{+0.14}$	16	3	1.21 ± 0.03	$0.83_{-0.22}^{+0.16}$
136.3	21	7	1.14 ± 0.02	$0.55_{-0.17}^{+0.14}$	10	3	1.23 ± 0.04	$0.92_{-0.27}^{+0.08}$

$e^+e^- \rightarrow \tau^+\tau^-(\gamma)$								
	total				high energy			
\sqrt{s} [GeV]	N_f	N_b	c	A_{fb}	N_f	N_b	c	A_{fb}
130.3	15	12	0.97 ± 0.02	$0.16_{-0.21}^{+0.16}$	10	2	1.17 ± 0.05	$0.65_{-0.25}^{+0.15}$
136.3	15	4	1.00 ± 0.02	$0.47_{-0.18}^{+0.14}$	11	1	1.17 ± 0.05	$0.98_{-0.23}^{+0.02}$

$e^+e^- \rightarrow e^+e^-(\gamma)$								
	total				high energy			
\sqrt{s} [GeV]	N_f	N_b	c	A_{fb}	N_f	N_b	c	A_{fb}
130.3	108	20	1.16 ± 0.05	0.80 ± 0.08	93	12	1.14 ± 0.05	0.88 ± 0.07
136.3	81	20	1.16 ± 0.05	0.70 ± 0.09	77	15	1.14 ± 0.05	0.77 ± 0.09

Table 3: Number of forward and backward events, correction factors and asymmetries of the reactions $e^+e^- \rightarrow \mu^+\mu^-(\gamma)$, $e^+e^- \rightarrow \tau^+\tau^-(\gamma)$ and $e^+e^- \rightarrow e^+e^-(\gamma)$ for the total and the high energy, $\sqrt{s'} > 110$ GeV, event samples. For the muon and tau-pair production an acollinearity angle cut of 90 degrees is applied. The electron-pair asymmetries are measured in $44^\circ < \theta < 136^\circ$ with an acollinearity angle cut of 60 degrees. For this channel an additional systematic error of 0.034 for the total and 0.037 for the high energy event sample is assigned.

$e^+e^- \rightarrow \gamma\gamma(\gamma)$				
\sqrt{s} [GeV]	\mathcal{L} [pb $^{-1}$]	N_{events}	$\sigma_{\gamma\gamma}^{\text{total}}$ [pb]	$\sigma_{\gamma\gamma}^{\text{QED}}$ [pb]
130.3	2.68	25	10.0 ± 2.0	8.5
136.3	2.29	16	7.5 ± 1.9	7.8

Table 4: Cross sections for the reaction $e^+e^- \rightarrow \gamma\gamma(\gamma)$ within the fiducial volume, $44^\circ < \theta_\gamma < 136^\circ$, and an acollinearity angle cut of $\xi < 60^\circ$. The QED prediction is calculated with the GGG Monte Carlo generator [18].

$e^+e^- \rightarrow \nu\bar{\nu}(\gamma)$						
			$E_\gamma > 3$ GeV, $20^\circ < \theta_\gamma < 160^\circ$	full phase space		
\sqrt{s} [GeV]	\mathcal{L} [pb $^{-1}$]	N_{events}	$\sigma_{\nu\bar{\nu}\gamma}$ [pb]	$\sigma_{\nu\bar{\nu}\gamma}^{\text{SM}}$ [pb]	$\sigma_{\nu\bar{\nu}}$ [pb]	$\sigma_{\nu\bar{\nu}}^{\text{SM}}$ [pb]
130.3	2.68	17	11.2 ± 2.7	14.1	95 ± 23	120
136.3	2.29	10	7.8 ± 2.5	12.0	68 ± 22	105

Table 5: Cross sections for the reaction $e^+e^- \rightarrow \nu\bar{\nu}(\gamma)$ with $E_\gamma > 3$ GeV and $20^\circ < \theta_\gamma < 160^\circ$ and extrapolated to full phase space. The Standard Model prediction is calculated with the KORALZ Monte Carlo generator [14].

Parameter	Treatment of Charged Leptons		Standard Model
	Non-Universality	Universality	
m_Z [MeV]	91196 ± 11	91196 ± 11	—
Γ_Z [MeV]	2494 ± 10	2493 ± 10	2498
$r_{\text{had}}^{\text{tot}}$	2.954 ± 0.029	2.953 ± 0.029	2.969
r_e^{tot}	0.1409 ± 0.0018	—	
r_μ^{tot}	0.1403 ± 0.0017	—	
r_τ^{tot}	0.1421 ± 0.0020	—	
r_ℓ^{tot}	—	0.1410 ± 0.0015	0.1427
$j_{\text{had}}^{\text{tot}}$	0.27 ± 0.41	0.29 ± 0.41	0.22
j_e^{tot}	-0.08 ± 0.11	—	
j_μ^{tot}	-0.023 ± 0.072	—	
j_τ^{tot}	0.046 ± 0.083	—	
j_ℓ^{tot}	—	-0.007 ± 0.050	0.004
r_e^{fb}	0.0016 ± 0.0019	—	
r_μ^{fb}	0.0031 ± 0.0012	—	
r_τ^{fb}	0.0047 ± 0.0017	—	
r_ℓ^{fb}	—	0.00318 ± 0.00085	0.00272
j_e^{fb}	0.68 ± 0.20	—	
j_μ^{fb}	0.81 ± 0.10	—	
j_τ^{fb}	0.70 ± 0.13	—	
j_ℓ^{fb}	—	0.749 ± 0.076	0.799
χ^2 / DOF	87/111	91/119	—

Table 6: Results on the S–Matrix parameters, derived with and without the assumption of lepton universality.

	m_Z	Γ_Z	$r_{\text{had}}^{\text{tot}}$	r_ℓ^{tot}	$j_{\text{had}}^{\text{tot}}$	j_ℓ^{tot}	r_ℓ^{fb}	j_ℓ^{fb}
m_Z	1.00	0.00	0.01	0.02	-0.55	-0.25	0.14	-0.03
Γ_Z		1.00	0.77	0.69	0.07	0.01	0.04	0.04
$r_{\text{had}}^{\text{tot}}$			1.00	0.88	0.04	-0.02	0.07	0.05
r_ℓ^{tot}				1.00	0.03	0.03	0.08	0.07
$j_{\text{had}}^{\text{tot}}$					1.00	0.24	-0.09	0.04
j_ℓ^{tot}						1.00	-0.01	0.14
r_ℓ^{fb}							1.00	0.15
j_ℓ^{fb}								1.00

Table 7: The correlation matrix for the 8 S–Matrix parameters derived with the assumption of lepton universality.

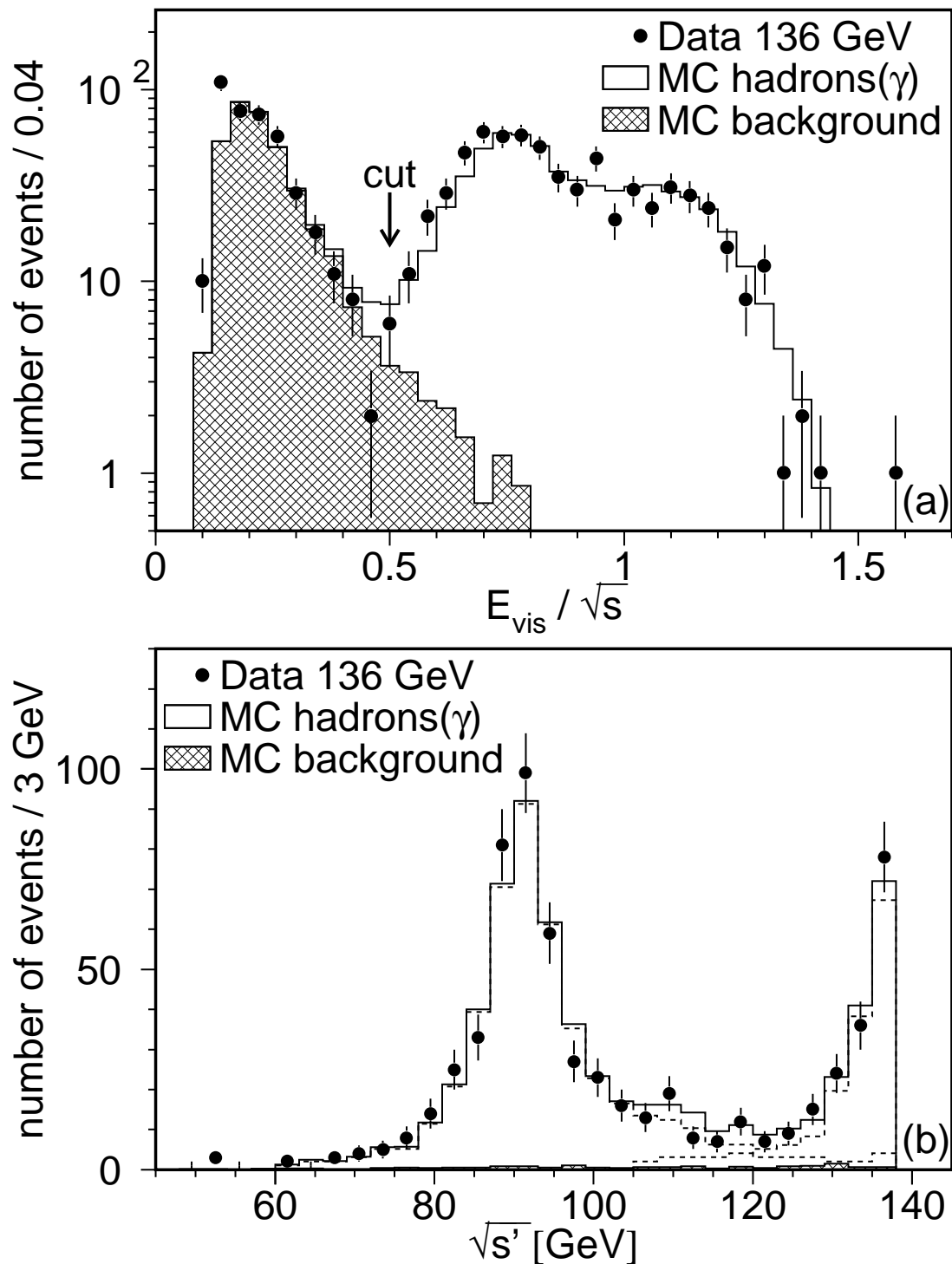


Figure 1: (a) The total visible energy, E_{vis} , normalised to the centre-of-mass energy, \sqrt{s} , for the selection of $e^+e^- \rightarrow \text{hadrons}(\gamma)$ events. The arrow indicates the position of the cut value. All other selection cuts have been applied. The background is dominated by two-photon collision processes. (b) The reconstructed $\sqrt{s'}$ distribution for $e^+e^- \rightarrow \text{hadrons}(\gamma)$ at 136 GeV, compared to the result of a fit determining simultaneously the cross sections below and above a $\sqrt{s'}$ value of 110 GeV. The Monte Carlo distributions of events generated below and above a $\sqrt{s'}$ value of 110 GeV are indicated by the dashed lines.

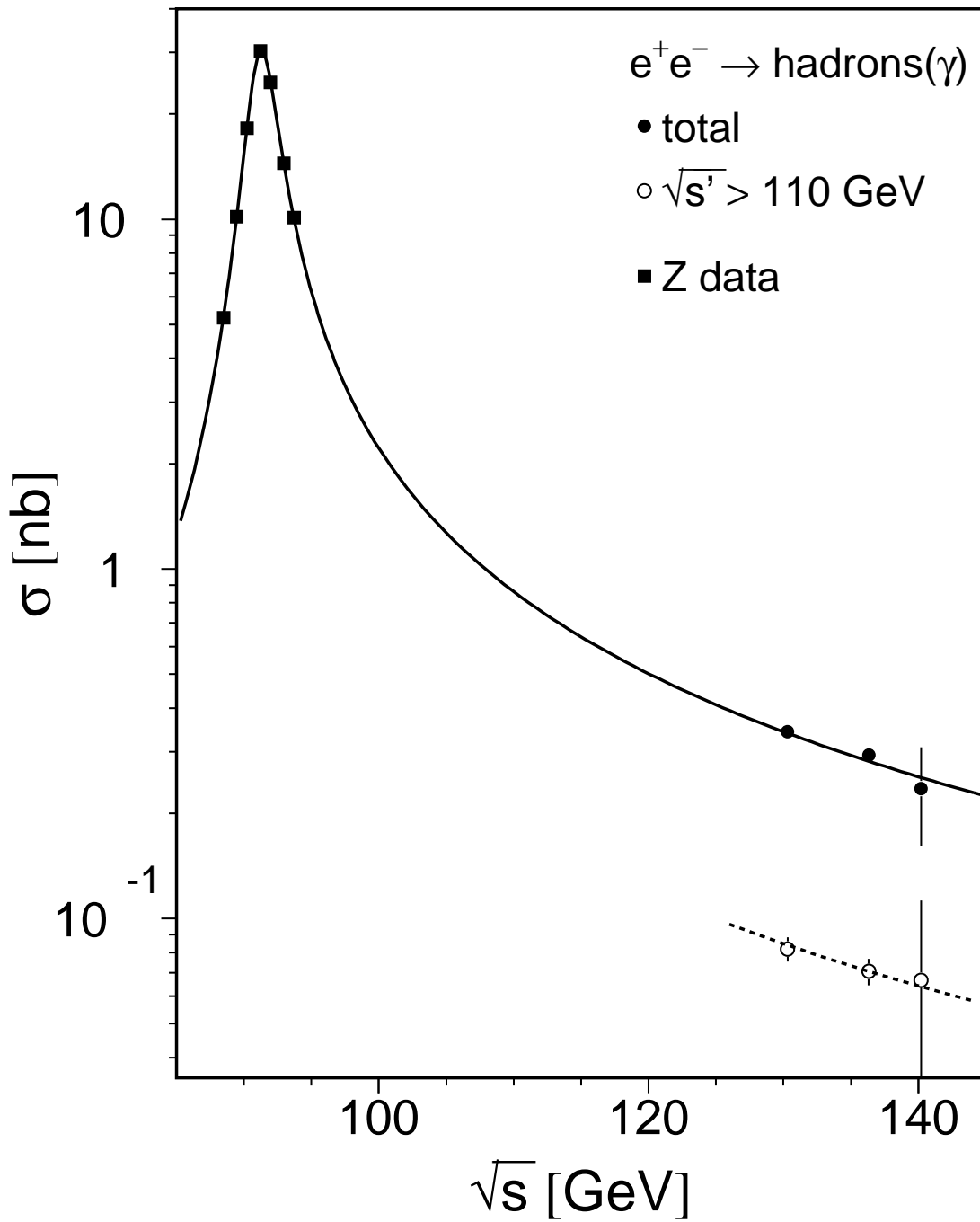


Figure 2: Cross section of the process $e^+e^- \rightarrow \text{hadrons}(\gamma)$ at energies between 130 GeV and 140 GeV for the total and the high energy event sample, $\sqrt{s'} > 110$ GeV. The solid line is the Standard Model prediction for the total cross section. The dashed line is the prediction for $\sqrt{s'} > 110$ GeV. Cross sections measured at the Z are also shown.

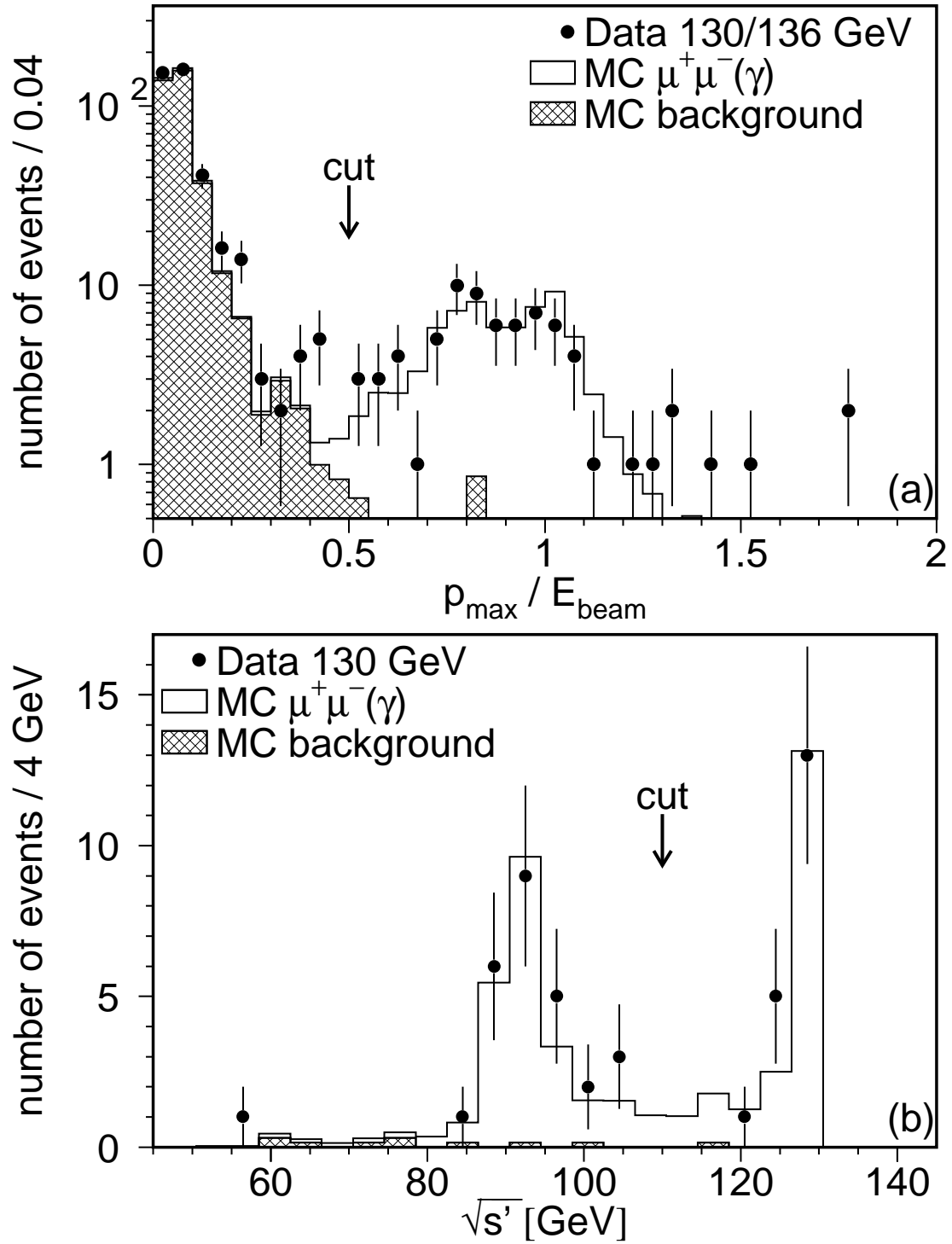


Figure 3: (a) The maximum reconstructed muon momentum, p_{\max} , normalised to the beam energy, E_{beam} , for the selection of $e^+e^- \rightarrow \mu^+\mu^-(\gamma)$ events. The arrow indicates the position of the cut value. All other selection cuts have been applied. The background shown is dominated by two-photon process $e^+e^- \rightarrow e^+e^-\mu^+\mu^-$. (b) The reconstructed $\sqrt{s'}$ distribution for the process $e^+e^- \rightarrow \mu^+\mu^-(\gamma)$ at 130 GeV. The arrow indicates the cut to isolate the high energy events.

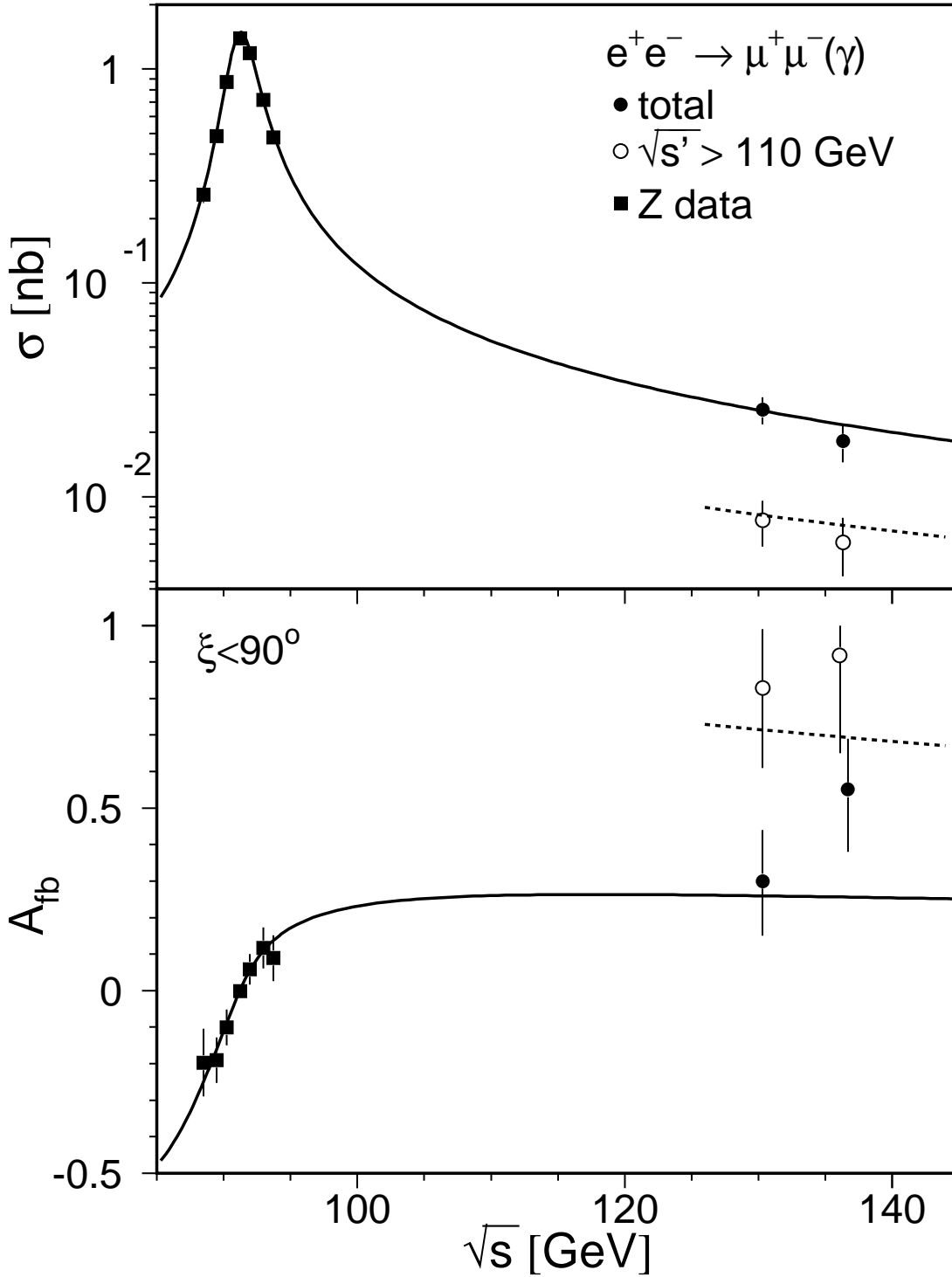


Figure 4: Cross section (top) and asymmetry for $\xi < 90^\circ$ (bottom) of the process $e^+e^- \rightarrow \mu^+\mu^-(\gamma)$ at energies of 130 GeV and 136 GeV for the total and the high energy event sample, $\sqrt{s'} > 110$ GeV. The solid lines are the Standard Model predictions for the total cross section and the asymmetry. The dashed lines are the predictions for $\sqrt{s'} > 110$ GeV. Cross sections and asymmetries measured at the Z are also shown. The asymmetries at the Z are corrected to account for the different acollinearity angle cut. When error bars overlap the \sqrt{s} values are slightly shifted for better visibility.

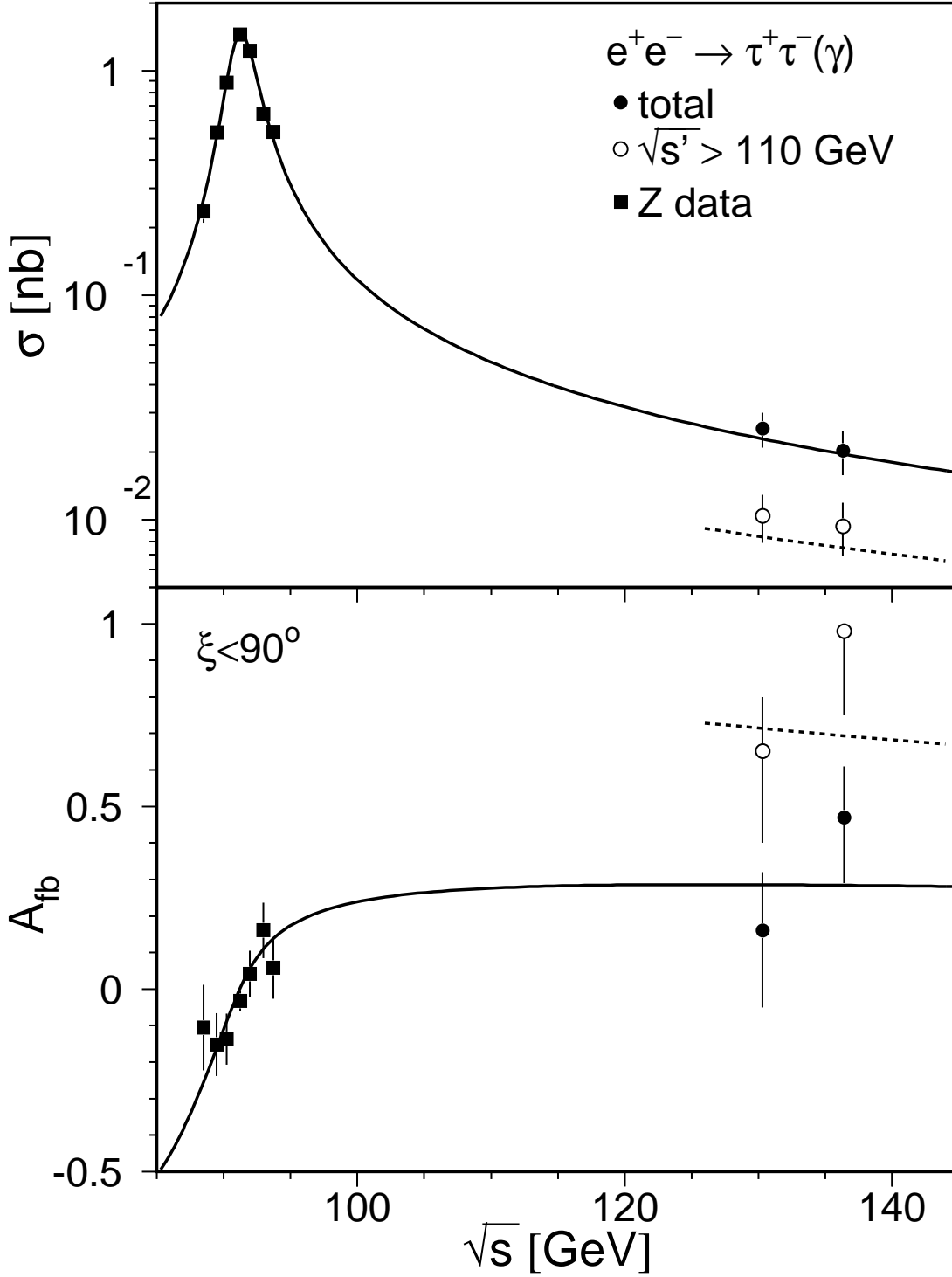


Figure 5: Cross section (top) and asymmetry for $\xi < 90^\circ$ (bottom) of the process $e^+e^- \rightarrow \tau^+\tau^-(\gamma)$ at energies of 130 GeV and 136 GeV for the total and the high energy event sample, $\sqrt{s'} > 110$ GeV. The solid lines are the Standard Model predictions for the total cross section and the asymmetry. The dashed lines are the predictions for $\sqrt{s'} > 110$ GeV. Cross sections and asymmetries measured at the Z are also shown. The asymmetries at the Z are corrected to account for the different acollinearity angle cut.

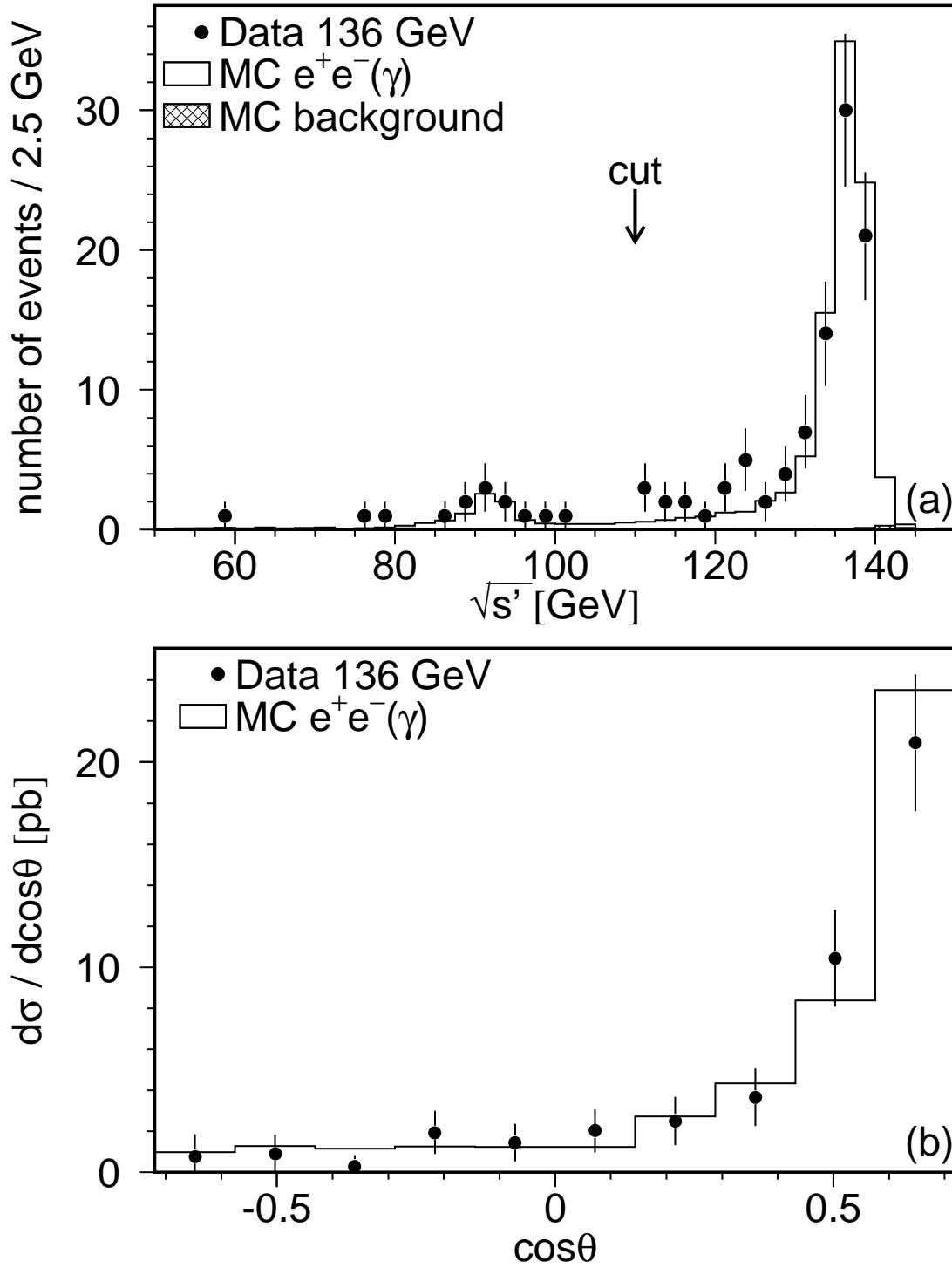


Figure 6: (a) The reconstructed $\sqrt{s'}$ distribution for the process $e^+e^- \rightarrow e^+e^-(\gamma)$ at 136 GeV. The arrow indicates the cut to isolate the high energy events. The background is dominated by the process $e^+e^- \rightarrow \gamma\gamma(\gamma)$. (b) The differential cross section for the high energy event sample, $\sqrt{s'} > 110$ GeV, of the process $e^+e^- \rightarrow e^+e^-(\gamma)$ at 136 GeV.

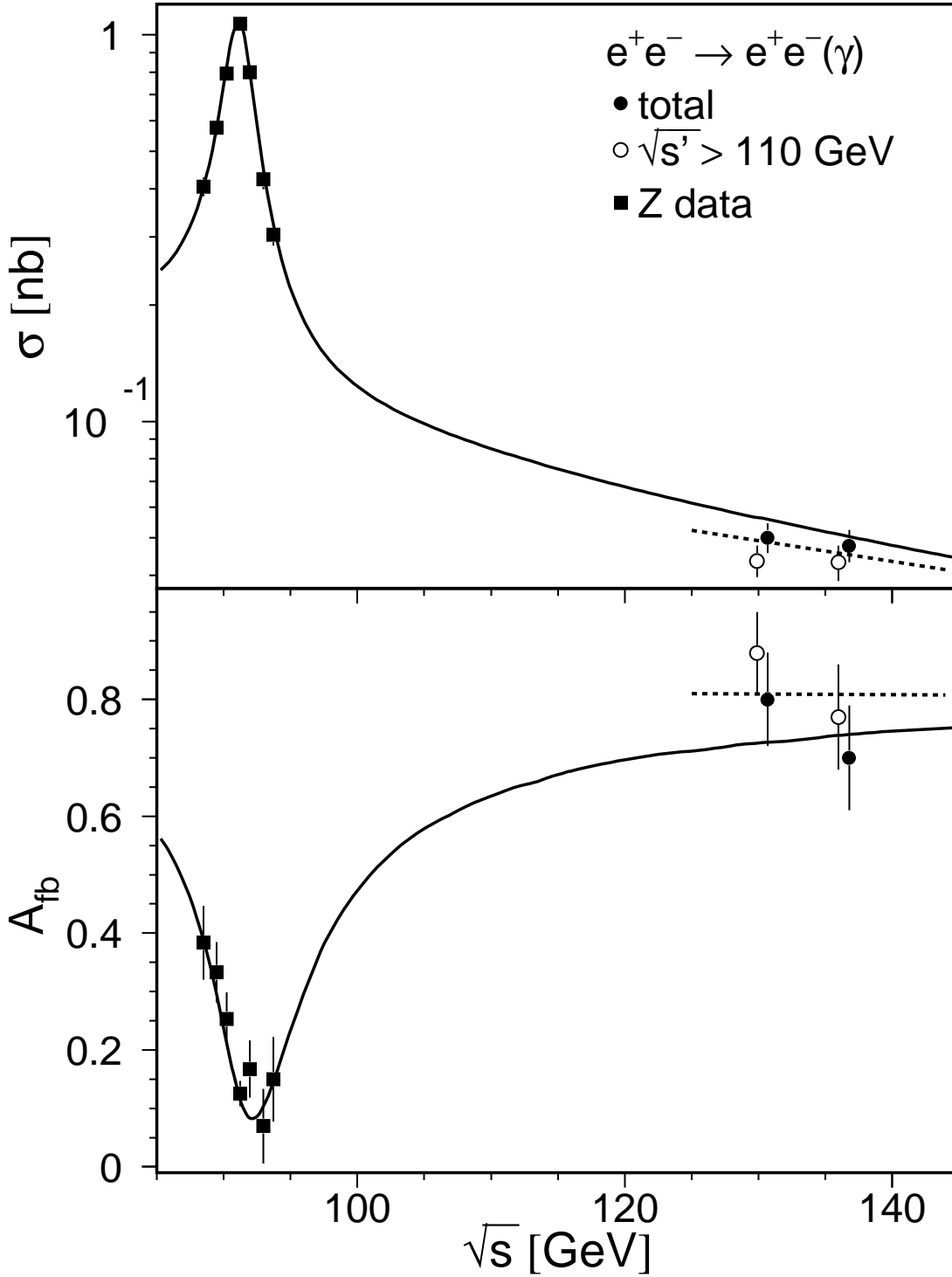


Figure 7: Cross section (top) and asymmetry (bottom) of the process $e^+e^- \rightarrow e^+e^-(\gamma)$ for both leptons inside $44^\circ < \theta < 136^\circ$ and an acollinearity angle cut of $\xi < 60^\circ$ at energies of 130 GeV and 136 GeV for the total and the high energy event sample, $\sqrt{s'} > 110$ GeV. The solid lines are the Standard Model predictions for the total cross section and the asymmetry. The dashed lines are the predictions for $\sqrt{s'} > 110$ GeV. Cross sections and asymmetries measured at the Z are also shown. They are corrected to account for the different acollinearity angle cut. When error bars overlap the \sqrt{s} values are slightly shifted for better visibility.

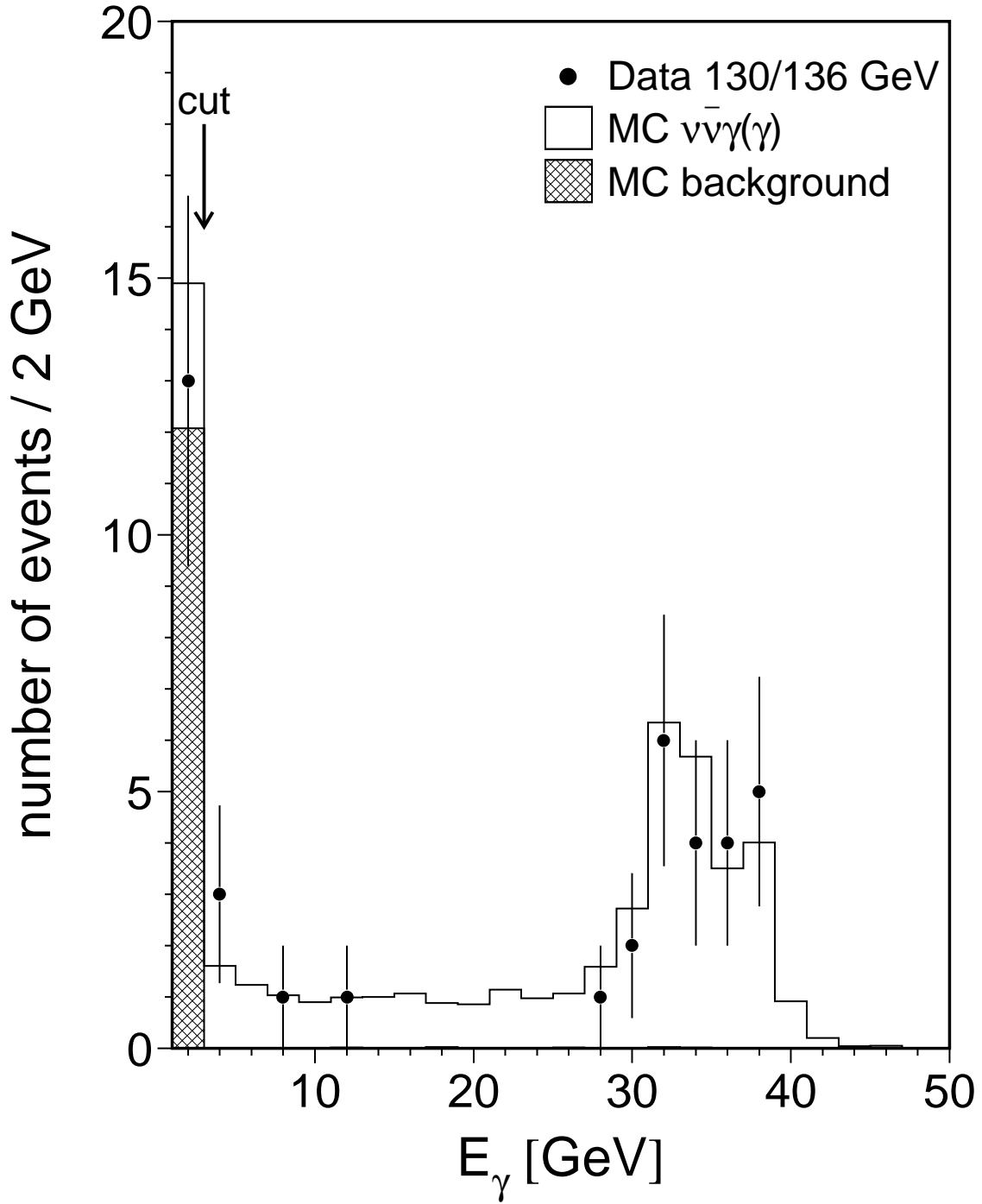


Figure 8: Energy, E_γ , of single photons in the process $e^+e^- \rightarrow \nu\bar{\nu}\gamma(\gamma)$ at \sqrt{s} of 130 GeV and 136 GeV. The background is dominated by the process $e^+e^- \rightarrow e^+e^-(\gamma)$.

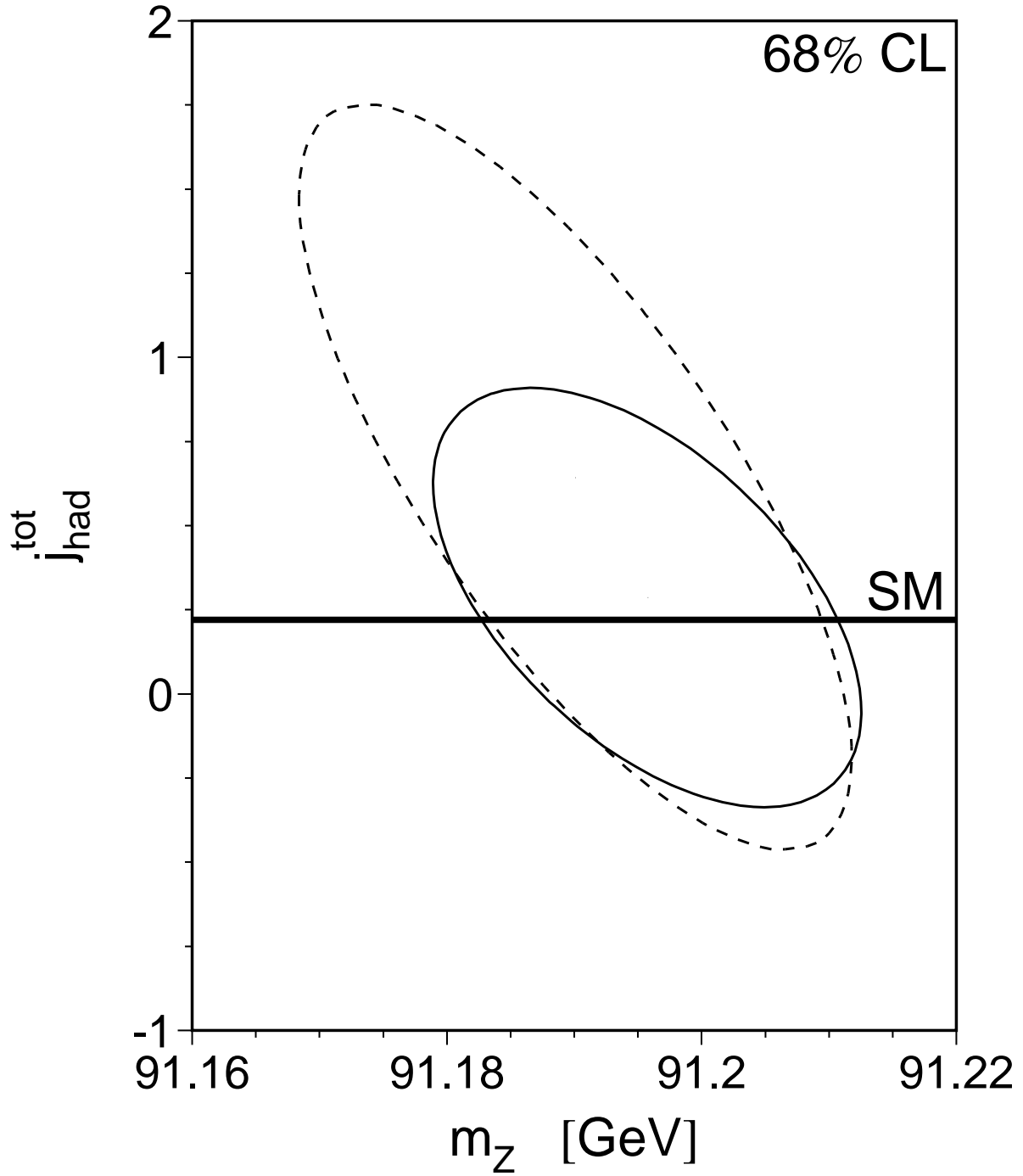


Figure 9: Contours in the $m_Z - j_{\text{had}}^{\text{tot}}$ plane at 68% confidence level under the assumption of lepton universality. The dashed line shows the Z data only whereas the solid line includes in addition the high energy data. The Standard Model prediction for $j_{\text{had}}^{\text{tot}}$ is shown as the horizontal band.